High-Resolution Conductivity Reconstruction by Electrical Impedance Tomography using Structure-Aware Hybrid-Fusion Learning

High-Resolution Conductivity Reconstruction by Electrical Impedance Tomography using Structure-Aware Hybrid-Fusion Learning

Hao Yu[a]*, Haoyu Liu[b], Zhe Liu[c], Zeyu Wang[d,e], Jiabin Jia[a,]*

[a] *Agile Tomography Group, School of Engineering, University of Edinburgh, Edinburgh, U.K.*

[b] *Mobile Intelligence Lab, School of Informatics, University of Edinburgh, Edinburgh, U.K.*

[c] *Intelligent Sensing, Analysis and Control Group, School of Engineering, University of Edinburgh, Edinburgh, U.K.*

[d] *Department of Neurosurgery, Xiangya Hospital, Center South University, Changsha, Hunan, P. R. China.*

[e] *Medical Research Council Centre for Regenerative Medicine, Institute for Regeneration and Repair, University of Edinburgh, Edinburgh, U.K.*

A B S T R A C T

Background: Electrical impedance tomography (EIT) has gained considerable attention in the medical field for the diagnosis of lung-related diseases, owing to its non-invasive and real-time characteristics. However, due to the ill-posedness and underdetermined nature of the inverse problem in EIT, suboptimal reconstruction performance and reduced robustness against the measurement noise and modeling errors are common issues.
Objectives: This study aims to mine the deep feature information from measurement voltages, acquired from the EIT sensor, to reconstruct the high-resolution conductivity distribution and enhance the robustness against the measurement noise and modeling errors using the deep learning method.
Methods: A novel data-driven method named the structure-aware hybrid-fusion learning (SA-HFL) network is proposed. SA-HFL is composed of three main components: a segmentation branch, a conductivity reconstruction branch, and a feature fusion module. These branches work in tandem to extract different feature information from the measurement voltage, which is then fused to reconstruct the conductivity distribution. The unique aspect of this network is its ability to utilize different features extracted from various branches to accomplish reconstruction objectives. To supervise the training of the network, we generated regular-shaped and lung-shaped EIT datasets through numerical calculations.
Results: The simulations and three experiments demonstrate that the proposed SA-HFL exhibits superior performance in qualitative and quantitative analyses, compared with five cutting-edge deep learning networks and the optical image-guided group sparsity (IGGS) method. The evaluation metrics, relative error (RE), mean structural similarity index (MSSIM), and peak signal-to-noise ratio (PSNR), are improved by implementing the SA-HFL method. For the regular-shaped dataset, the values are 0.119 (RE), 0.9882 (MSSIM), and 31.03 (PSNR). For the lung-shaped dataset, the values are 0.257 (RE), 0.9151 (MSSIM), and 18.67 (PSNR). Furthermore, the proposed network can be executed with appropriate parameters and efficient floating-point operations per second (FLOPs), concerning network complexity and inference speed.
Conclusions: The reconstruction results indicate that fusing feature information from different branches enhances the accuracy of conductivity reconstruction in the EIT inverse problem. Moreover, the study shows that fusing different modalities of information to reconstruct the EIT conductivity distribution may be a future development direction.

Keywords: Electrical impedance tomography, Lung disease diagnosis, Hybrid-fusion learning, Conductivity reconstruction and Robustness enhancement

1. Introduction

Electrical impedance tomography (EIT) is an emerging and promising medical imaging modality that has rapidly developed over the past two decades [1–3]. Compared with computed tomography (CT) [4] and magnetic resonance imaging (MRI) [5], EIT provides the advantages of being radiation-free, non-invasive and providing real-time imaging, enabling bedside assessment for patients [6]. As a result, it has gained significant attention in the diagnosis of various clinical diseases, particularly in the field of lung disease diagnosis [7,8]. EIT enables doctors to assess the respiratory conditions of patients by monitoring dynamic changes in the conductivity distribution of lung tissues. The presence of lesions in lung tissue would result in abnormal conductivity distribution within the affected areas, which aids in the diagnosis of various pulmonary diseases [9], such as pulmonary edema, pleural effusion, and pneumothorax.

EIT measures boundary voltage through sensors placed on the surface of the chest and reconstructs the conductivity distribution in different regions of the lung by solving the inverse problem [10]. However, in the reconstruction process, EIT suffers from poor robustness and inaccurate reconstruction for the reasons of the nonlinear, highly ill-posed, and underdetermined nature of the EIT inverse problem [11,12]. This inherently ill-posed process means that even minor inaccuracies in measurements, or modeling errors can lead to substantial artifacts in the reconstructed conductivity distribution [13]. To cope with the problem, both iterative optimization methods and noniterative methods are commonly employed. Despite the typically superior reconstruction results of iterative optimization methods, they present challenges in terms of imaging speed. On the other hand, while the imaging quality of noniterative methods may be limited, their imaging speed greatly surpasses that of the iterative methods. Representative iterative algorithms include total variation (TV) [14] and structure-aware sparse Bayesian learning (SA-SBL) [15]. For noniterative algorithms, Tikhonov [16] and Newton's one-step error reconstructor (NOSER) [17] are the state-of-the-art methods. However, the nonlinear and underdetermined properties remain as significant obstacles in solving the EIT inverse problem, which to some extent, hinders its clinical applicability.

Recently, deep learning methods have attracted much attention from scholars, proving to be an effective way to address the EIT problems mentioned above [18–21]. The purpose of deep learning-based methods is to minimize loss by finding the optimal weights and biases of the trained model. The "Image-to-image" deep learning method is a classic approach to tackling the EIT problem [22]. However, it does not fully utilize the information from EIT sensors. In contrast, the "Sequence-to-image" (data-driven) method seems to be more suitable for the EIT inverse problem, as it can fully utilize the original information obtained from the sensor array [19].

Wu *et al*. established a nonlinear mapping between measurement voltages and conductivity distribution by integrating the convolutional neural network (CNN) with the radial basis function (RBF) [23]. However, the use of a fully connected layer at the end disrupts the spatial correlation of the conductivity distribution. Chen *et al*. proposed a novel fully connected-UNet (FC-UNet) for cell imaging [24]. Ren *et al*. introduced a two-stage deep learning (TSDL) structure, consisting of a pre-reconstruction block and a CNN post-processing block, to reconstruct high-resolution lung images and improve robustness against modeling errors [25]. Additionally, various networks, such as the error-constraint network (Ec-Net) [26], improved LeNet [27] and the feed-forward fully connected artificial neural network (FFFC-ANN) [28] have been applied to EIT for conductivity reconstruction. Structure-aware dual-branch network (SADB-Net) [29] was proposed by Chen *et al*. in cell imaging. However, the information fusion method by the fully connected concatenation approach disrupts the spatial correlation of the conductivity distribution. Additionally, the inclusion of a pre-training round further complicates the parameter adjustment process. Despite these efforts from scholars, there is still room for improving both reconstruction performance and robustness in EIT conductivity tasks. Conductivity reconstruction should be viewed as a downstream task of imaging reconstruction, focusing primarily on conductivity values rather than pixel recovery. Existing methodologies, such as [23,24,26–28], tend to create a direct mapping from voltage measurements to the conductivity distribution, omitting the intermediate binary maps. These approaches inevitably introduce errors during the training process.

Inspired by the optical image-guided group sparse (IGGS) method [30], which employs photoelectric dual-modality for reconstruction, this paper aims to employ a single-modality approach to simulate dual-modal capabilities. Specifically, the paper seeks to decouple the structural information and conductivity distribution from the measured voltages. Using deep learning methods, feature extraction is performed on these decoupled data to reconstruct the conductivity distribution. We employ an intermediate branch dedicated to learning the binary masks from the given inputs by a specific loss function. These binary maps are then fused into the subsequent task of conductivity reconstruction. By incorporating this design, we maintain the integrity of the end-to-end machine learning training routine while introducing a supplementary objective to enhance the learning of signals through back-propagation. The contributions of our work are as follows,

1. A structure-aware hybrid-fusion learning (SA-HFL) end-to-end network is proposed to achieve high-resolution conductivity distribution reconstruction and enhance robustness against measurement noise and modeling errors.
2. The proposed network enhances the EIT reconstruction by decoupling and extracting structural and conductivity information from measurement voltages, achieving structure preservation and accurate conductivity through specialized branches and the loss function.
3. Compared to other advanced deep learning networks and the IGGS method, the SA-HFL demonstrates superior performance in terms of relative error, mean structural similarity index, and peak signal-to-noise ratio.
4. Preliminary results from both simulations and real-world experiments substantiate the feasibility and superior efficacy of the SA-HFL for practical EIT reconstruction tasks.

In our work, an efficient dual branch structure-aware hybrid-fusion learning (SA-HFL) network is proposed to establish the nonlinear mapping between the boundary voltages and medium distribution. The SA-HFL consists of a segmentation branch and a conductivity reconstruction branch. Each branch focuses on different features: the segmentation branch on structural features and the conductivity reconstruction branch on conductivity features, which are achieved by distinct loss functions. By fusing the differentiated feature information extracted from each branch, the results encapsulate more dimensional information, thereby achieving superior reconstruction performance and robustness against measurement noise and modeling errors. The effectiveness of the proposed network in reconstructing the conductivity distribution is demonstrated through simulations and three different experiments, where it is compared with five competitive deep learning and the IGGS methods.

2. Method

2.1 Mathematical Model of EIT

In EIT, for a given bounded imaging domain Ω, when the excitation current $\mathbf{I}(x,y)$ is injected into the domain, the relationship between the conductivity distribution $\boldsymbol{\sigma}(x)$ and the

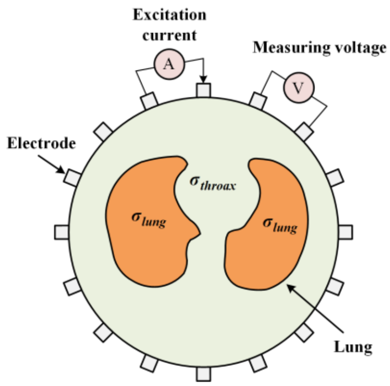

Fig. 1. Adjacent excitation and measurement patterns of the EIT system.

induced potential distribution $\mathbf{u}(x,y)$ can be obtained by the following complete electrode model (CEM) [31,32], that is,

$$\nabla \cdot (\boldsymbol{\sigma}(x,y)\nabla \mathbf{u}(x,y)) = 0, \quad x, y \in \Omega \tag{1}$$

where the boundary conditions satisfy the following relationship,

$$\begin{gathered}
\mathbf{u}(x,y) + z_l \boldsymbol{\sigma}(x,y)\frac{\partial \mathbf{u}(x,y)}{\partial n} = U_l, \quad x, y \in e_l, l = 1,\ldots,L \\
\int_{e_l} \boldsymbol{\sigma}(x,y)\frac{\partial \mathbf{u}(x,y)}{\partial n} dS = I_l, \quad l = 1,\ldots,L \\
\boldsymbol{\sigma}(x,y)\frac{\partial \mathbf{u}(x,y)}{\partial n} = 0, \quad x, y \in \partial\Omega \setminus \bigcup_{l=1}^{L} \\
\sum_{l=1}^{L} I_l = 0, \quad \sum_{l=1}^{L} U_l = 0
\end{gathered} \tag{2}$$

where z_l is the contact impedance, e_l is the l-th sensor on the boundary, L is the number of electrodes, which is 16 in the paper, and U_l and I_l are the measurement voltage and excitation current on the l-th electrode respectively. In this work, the neighboring bipolar pattern is adopted, and the forward problem is solved using the finite element method (FEM) [33]. The working principle of the EIT system is shown in Fig. 1.

In addition to the forward problem mentioned above, the inverse problem is also a critical step in EIT. The inverse problem, which aims to reconstruct the conductivity distribution from the boundary voltage, can be described by the following equation,

$$\mathbf{V} = F(\boldsymbol{\sigma}) + \mathbf{e} \tag{3}$$

where $F(\cdot)$ is the nonlinear forward operator, $\mathbf{V}$ is the measurement voltage and $\mathbf{e}$ is the measurement noise.

In the paper, the inverse problem is solved by the deep learning method, which can be expressed as follows,

$$f_{EIT} = \arg\min \frac{1}{N}\sum_{k=1}^{N} \left\| f_{EIT}(\mathbf{V}) - \boldsymbol{\sigma}_{\mathbf{Act}} \right\|_2^2 + \mathrm{Reg}(\theta) \tag{4}$$

where f_{EIT} is the EIT network function used to learn the network weights and biases between the measurement voltage $\mathbf{V}$ and the actual conductivity distribution $\boldsymbol{\sigma}_{\mathbf{Act}}$. $\mathrm{Reg}(\theta)$ represents the regularization operation. N is the number of actual conductivity distribution $\boldsymbol{\sigma}_{\mathbf{Act}}$.

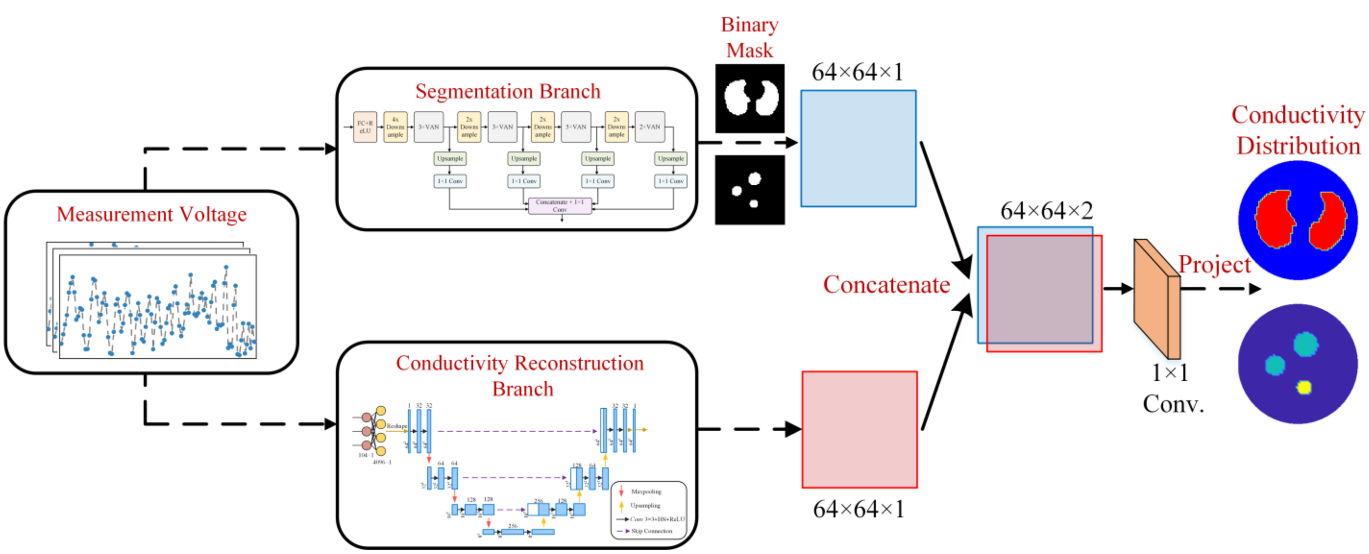

Fig. 2. Architecture of the Structure-Aware Hybrid-Fusion Learning Network.

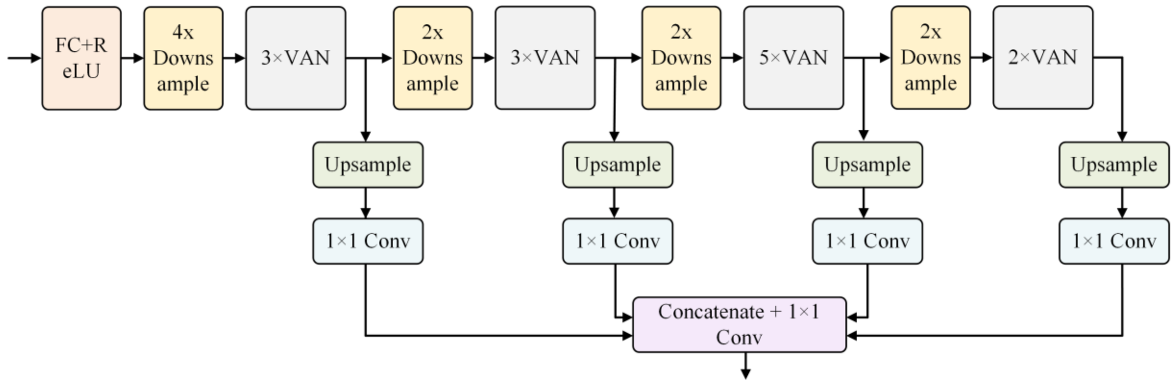

Fig. 3. Architecture of the segmentation branch.

2.2 The Architecture of the Structure-Aware Hybrid-Fusion Learning Network

As shown in Fig. 2, the architecture of the SA-HFL consists of two branches: the segmentation branch, which is used to obtain the binary mask of the object, and the conductivity reconstruction branch, which is used to reconstruct the initial conductivity distribution. After the corresponding branch information is extracted, the two features are fused by concatenation operation, followed by a 1 × 1 convolution kernel to obtain the final conductivity distribution.

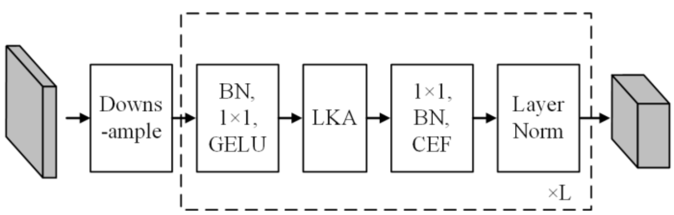

(a) A stage of VAN

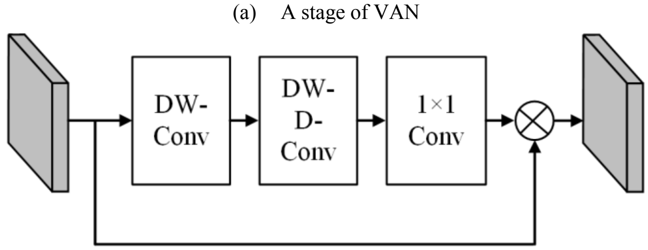

(b) LKA

Fig. 4. Module structure of the segmentation branch. (a) A stage of VAN, (b) Large Kernel Attention.

Table 1
The dimension changes of data matrix of the segmentation branch.

Step	Layers	Output size
Input	3228 FC + ReLU + Padding + Reshape	64 × 64 × 1
2-1	4x Downsample + 3×VAN	16 × 16 × 32
2-2	Upsample + 1× 1 Conv.	64 × 64 × 1
3-1	2x Downsample + 3×VAN	8 × 8 × 64
3-2	Upsample + 1× 1 Conv.	64 × 64 × 1
4-1	2x Downsample + 5×VAN	4 × 4 × 160
4-2	Upsample + 1× 1 Conv.	64 × 64 × 1
5-1	2x Downsample + 2×VAN	2 × 2 × 256
5-2	Upsample + 1× 1 Conv.	64 × 64 × 1
Output	Concatenate + 1× 1 Conv.	64 × 64 × 1

*Height×Width×Channel

2.2.1 Architecture of the segmentation branch

This paper employs the visual attention network (VAN) [34] as the backbone for the segmentation branch. As depicted in Fig. 3, the architecture of this branch follows a hierarchical structure. The input, a 104 × 1 vector representing the measurement voltage, is passed through a 3228-dimension fully connected (FC) layer and a rectified linear unit (ReLU) activation function to yield an initial guess of the binary mask. To extract deeper features, the 3228 × 1 initial guess, augmented with additional padding, is reshaped into a 64 × 64 two-dimensional feature map, followed by a downsampling layer with a stride of 4 and 3 VAN modules. In the direction of upsampling propagation, a binary mask is obtained using a combination of a 2 × 2 upsampling layer and a 1 × 1 convolution kernel. In the direction of downsampling, the aforementioned operations are repeated three times.

Finally, binary masks that contain information from various depths and scales are derived. By concatenating these binary masks and utilizing a 1 × 1 convolutional kernel to adjust the channel count, the binary mask of the object, a 64 × 64 × 1 matrix, can be obtained. The changes in the dimensions of the data matrix throughout this process are detailed in Table 1.

The backbone structure of the VAN module, as shown in Fig. 4 (a), comprises a cascade of components: a batch normalization (BN) layer, a 1 × 1 convolutional kernel, the Gaussian error linear unit (GELU) [35] activation function, the large kernel attention (LKA) module, a 1 × 1 convolution layer, a BN, a convolutional feed-forward network (CFF) [36] and a layer normalization layer [37].

The GELU activation function is defined as follows,

$$GELU(x) = x \times [1 + erf(x/\sqrt{2})] \tag{5}$$

where $erf(\cdot)$ is the Gauss error function.

To address the computational burden posed by large convolution kernels while fully leveraging the benefits of the self-attention mechanism and large convolution kernels, such as local voltage information, large receptive fields, and dynamic processes, the LKA module utilizes the decomposition of large convolution kernels to capture long-range relations.

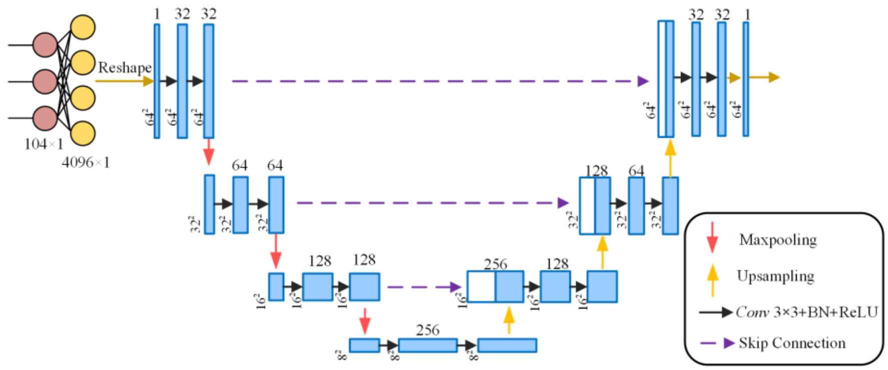

Fig. 5. Architecture of the conductivity reconstruction branch.

The structure of the LKA module, as shown in Fig. 4 (b), is constructed with a 5 × 5 depth-wise convolution (DW-Conv), a 7 × 7 depth-wise dilation convolution (DW-D-Conv) with a dilation of 3, and a 1 × 1 convolutional kernel. The mathematical expression of the LKA module is as follows,

$$LKA(F) = Conv_{1\times1}(DW\text{-}D\text{-}Conv(DW\text{-}Conv(F))) \otimes F \quad (6)$$

where the attention scores, i.e., the convolution operation results, represent the importance of different features, and F is the input feature map of the LKA module. Symbol $\otimes$ denotes the element-wise multiplication operation. It is worth noting that the LKA module achieves adaptability not only in the spatial dimension but also in the channel dimension. By incorporating the LKA module into the VAN architecture, it is possible to effectively extract local information and facilitate interactions between local and remote information, resulting in a better information extraction effect.

2.2.2 Architecture of the conductivity reconstruction branch

The design of the conductivity reconstruction branch takes inspiration from the UNet framework [38]. This branch is composed of an encoder and a decoder that have the ability to capture the conductivity information from the EIT sensor matrix. The progression of data dimensions and the structure of the network are depicted in Fig. 5. The input voltage undergoes an initial process through a fully connected layer with 4096 dimensions, which is subsequently reshaped into a 64 × 64 × 1 data matrix through a reshape operation. After the initial data preprocessing stage, the 64 × 64 × 1 matrix is passed through the UNet network. Finally, an initial estimation of the conductivity distribution is obtained.

2.2.3 Feature fusion

The segmentation branch and the conductivity reconstruction branch are tasked with learning the structural and conductivity information of the measured object, respectively. These two aspects are integrated via a channel-wise concatenation operation. This amalgamated 64 × 64 × 2 matrix is then subjected to fusion through a 1 × 1 convolution kernel, culminating in a final conductivity distribution following a clipping operation.

By employing a hybrid information fusion approach, which combines the structure-aware features with conductivity distribution characteristics, the network is enabled to learn deeper and more scalable information. As a result, both the reconstruction capabilities and the robustness of the network are substantially enhanced.

2.3 Loss function

The total loss consists of three distinct parts: segmentation loss, conductivity reconstruction loss, and l_2 regularization loss. The expression for the loss function is as follows,

$$\mathrm{L}_{Total} = \alpha \mathrm{L}_{BBCE} + \mathrm{L}_{Cond} + \lambda \|\theta\|^2 \quad (7)$$

here, $\mathcal{L}_{BBCE}$ represents the balanced binary cross-entropy (BBCE) [39], while $\mathcal{L}_{Cond}$ denotes the mean square error (MSE) loss. α is the weighting factor.

For the segmentation branch, the definition of BBCE loss is given by,

$$\begin{aligned}\mathrm{L}_{BBCE}(\mathbf{W},\mathbf{w}) = &-\beta \sum_{j\in Y_+} ln\, Pr\left(y_j = 1 | X;\mathbf{W},\mathbf{w}\right) - \\ &(1-\beta)\sum_{j\in Y_0} ln\, Pr\left(y_j = 0 | X;\mathbf{W},\mathbf{w}\right)\end{aligned} \quad (8)$$

where β represents the proportion of pixels at 0 in the total number of pixels. Y_+ and Y_0 denote the region of interest (ROI) and non-ROI label sets, respectively. j is the index that iterates over the spatial dimensions of conductivity distribution X. Pr $(y_j = 1| X; \mathbf{W}, \mathbf{w})$ is the prediction probability of the object region, conversely, Pr $(y_j = 0| X; \mathbf{W}, \mathbf{w})$ is the probability of the non-object region.

For the conductivity reconstruction branch, the loss function $\mathcal{L}_{Cond}$ is given by,

$$\mathrm{L}_{Cond} = \frac{1}{N}\sum_{i}^{N} \left\| \boldsymbol{\sigma}_{\mathbf{Act}} - \boldsymbol{\sigma}_{\mathbf{Rec}} \right\|^2 \quad (9)$$

where N is the number of actual conductivity distribution $\boldsymbol{\sigma}_{\mathbf{Act}}$, which is 3228 in the work and $\boldsymbol{\sigma}_{\mathbf{Rec}}$ is the reconstructed conductivity distribution.

Finally, the third term of (7) is l_2 regularization, which is adopted to address the problem of overfitting, and θ represents the trained parameters of the network.

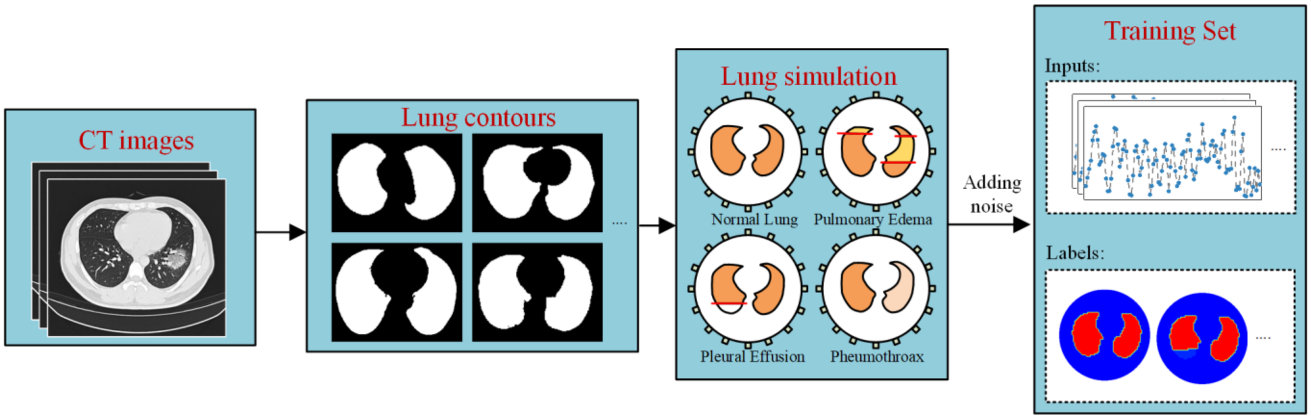

Fig. 6. Generation of lung-shaped EIT dataset.

2.4 Quantitative analysis metrics

In this paper, model parameters and floating-point operations per second (FLOPs) are utilized to quantitatively evaluate the total number of trainable parameters in the model and the computational complexity of the model, respectively.

In addition, relative error (RE), mean structural similarity indices (MSSIM), and peak signal-to-noise ratio (PSNR) are adopted in the paper to quantitatively analyze the quality of the conductivity reconstruction performance, and RE is given by,

$$\mathrm{RE} = \frac{\left\| \boldsymbol{\sigma}_{\mathrm{Rec}} - \boldsymbol{\sigma}_{\mathrm{Act}} \right\|}{\left\| \boldsymbol{\sigma}_{\mathrm{Act}} \right\|} \tag{10}$$

A smaller RE indicates a better prediction result.

Furthermore, the definition of MSSIM is as follows,

$$\mathrm{MSSIM} = \frac{1}{K}\sum_{r}\sum_{c}\left[\frac{(2\overline{\boldsymbol{\sigma}_{\mathrm{Act\_L}}}\,\overline{\boldsymbol{\sigma}_{\mathrm{Rec\_L}}}+C_1)}{(\overline{\boldsymbol{\sigma}_{\mathrm{Act\_L}}}^2+\overline{\boldsymbol{\sigma}_{\mathrm{Rec\_L}}}^2+C_1)}\times \frac{(2Cov\left(\boldsymbol{\sigma}_{\mathrm{Act\_L}},\boldsymbol{\sigma}_{\mathrm{Rec\_L}}\right)+C_2)}{(Var(\boldsymbol{\sigma}_{\mathrm{Act\_L}})^2+Var(\boldsymbol{\sigma}_{\mathrm{Rec\_L}})^2+C_2)}\right] \tag{11}$$

where $Cov(\cdot)$ and $Var(\cdot)$ represent the mathematical operations for covariance and variance, respectively. $\boldsymbol{\sigma}_{\mathrm{Rec\_L}}$ is the local reconstructed conductivity distribution, while $\boldsymbol{\sigma}_{\mathrm{Act\_L}}$ denotes the local actual conductivity distribution. Furthermore, r and c are pixel position indexes within the conductivity distribution, and K denotes the number of local windows present in the conductivity distribution. The constants C_1 and C_2 are defined with values of 0.01 and 0.03. A value of MSSIM closer to 1 indicates greater similarity between the actual and reconstructed conductivities.

PSNR is used in the paper to measure the quality of the reconstructed conductivity distribution compared to its original version,

$$\mathrm{PSNR} = 10 \cdot log_{10} \frac{\left(Max(\boldsymbol{\sigma}_{\mathrm{Act}})\right)^2}{\mathrm{MSE}} \tag{12}$$

where MSE is the mean squared error between the actual conductivity distribution and the reconstructed conductivity distribution, defined as follows,

$$\mathrm{MSE} = \frac{1}{N}\sum_{i}^{N}\left\| \boldsymbol{\sigma}_{\mathrm{Act}} - \boldsymbol{\sigma}_{\mathrm{Rec}} \right\|^2 \tag{13}$$

3. Training setup

3.1 Data generation

(1) Regular-shaped EIT dataset

The regular-shaped EIT dataset comprises scenarios with one, two, and three circles, and inclusions are randomly distributed within the domain. Moreover, the dataset includes diverse combinations of circles and triangles, circles and squares, triangles and squares, as well as mixtures of all three shapes. Among them, squares and triangles have different rotation angles, 60° and 90° respectively. The inclusions are randomly assigned as either insulating or metallic materials, with conductances set to 0.001 S/m and 1 S/m, respectively. After obtaining the simulation data, the dataset is randomly divided into a training set and a test set at the ratio of 9:1. The size of the training set is 52200 and that of the test set is 5800.

(2) Lung-shaped EIT dataset

CT lung images of 18 patients are selected from the Cancer Imaging Archive (TCIA) open database as the basis for simulating boundary voltages for the lung-shaped EIT dataset. The steps for generating the dataset are illustrated in Fig. 6. After obtaining CT images, the global thresholding image segmentation algorithm is applied to extract the lung contours, which are then used to simulate normal lung and various

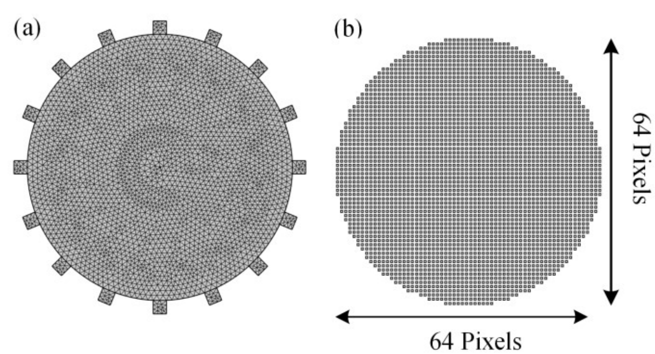

Fig. 7. Examples for adopted forward and inverse FEM meshes. (a) Forward mesh consisting of 5598 domain and 288 boundary elements for circular model, (b) inverse mesh consisting of 3228 elements for circular model

pulmonary diseases: pulmonary edema, pleural effusion, and pneumothorax. Conductivity distribution varies for different lung diseases [9]. Through manual rigid transformation: scaling, rotation, and translation operations make the chest contour coincide with the circle or thorax domain in the x direction as much as possible, thereby merging the lungs into the model. In the pulmonary edema model, tissue lesions cause an imbalance in the generation and reflux of tissue fluid in the lungs, leading to abnormally high and uneven distribution of lung conductivity. Pleural effusion, the pathological accumulation of fluid in the pleural space, results in a high-conductivity region within the lung [40]. In the pneumothorax model, the conductivity of the left or right lung is abnormal due to the presence of gas in the pleural cavity. As referenced in [41], the background conductivity is set to 0.48 S/m, while the conductivity of the lung area is set to 0.12 S/m.

In accordance with the characteristics of different lung diseases, the conductivity of the ROI is linearly changed to construct the dataset. The sizes of the training set and test set are 22499 and 3476, respectively. The inputs of the dataset are boundary voltages and the labels are the conductivity distribution of the reconstructed area. In order to improve the robustness of the network, which is crucial for maintaining the stability of the network, training data are augmented appropriately. Gaussian white noise (GWN) is added in boundary voltages with a 45 dB signal-to-noise ratio (SNR). The joint simulation is executed based on COMSOL$^{@}$ and MATLAB. Examples of the adopted forward and inverse FEM meshes are depicted in Fig. 7. For the forward problem of the circular homogeneous model, the mesh consists of 5598 domain and 288 boundary elements. For the inverse problem, the mesh consists of 3228 elements for the circular model.

3.2 Data normalization

To enhance the accuracy and speed of the training model, while simultaneously preventing the gradient explosion phenomenon in the deep learning training process, the measurement voltage and conductivity label could be pre-normalized. Data pre-processing can mitigate the effects caused by data collection errors of the EIT system and improve the generalization ability of the model. The normalization process is as follows,

$$\begin{aligned} \mathbf{V}_{\mathbf{Norm}} &= \frac{\mathbf{V}_{\mathbf{Mea}} - \mathbf{V}_{\mathbf{Ref}}}{\mathbf{V}_{\mathbf{Ref}}} \\ \boldsymbol{\sigma}_{\mathbf{Norm}} &= -\frac{\boldsymbol{\sigma}_{\mathbf{Act}} - \boldsymbol{\sigma}_{\mathbf{Ref}}}{\boldsymbol{\sigma}_{\mathbf{Ref}}} \end{aligned} \tag{14}$$

where $\mathbf{V}_{\mathbf{Mea}}$ and $\boldsymbol{\sigma}_{\mathbf{Act}}$ denote the measurement voltage and actual conductivity distribution when the targets are present; $\mathbf{V}_{\mathbf{Ref}}$ and $\boldsymbol{\sigma}_{\mathbf{Ref}}$ denote the reference voltage and reference conductivity distribution in the case of a homogeneous medium; $\mathbf{V}_{\mathbf{Norm}}$ and $\boldsymbol{\sigma}_{\mathbf{Norm}}$ are the voltage and conductivity distribution after normalization. The conductance of insulating materials is close to 0, which makes it difficult to distinguish when displayed after normalization. For this reason, it is mapped to 0.5. Metals are mapped to 1.

3.3 Baseline and training setup

In this study, we strive to conduct a thorough quantitative comparison between various methods to demonstrate the superior reconstruction capacity of our proposed network. To this end, we have selected five learning-based methods and one iterative bimodal fusion approach--IGGS method as benchmarks. The learning-based methods include Improved LeNet [27], CNN-RBF [23], UNet [38], Ec-net [26] and SADB-Net [29]. These selected methods serve as six baselines for comparison, illuminating the advancements made by our proposed network in the context of existing state-of-the-art approaches.

For the deep learning methods, the Adam optimizer is employed. The maximum training epoch is set to 100, with an exponential decay of 0.98 applied at each epoch. The l_2 regularization parameter is set to 1×10^{-5}. For the SADB-Net, the same supervision strategy mentioned in [29] is adopted. The disparate data convergence attributes of the network call for distinct training durations for each dataset. Thus, the lung-shaped dataset undergoes pre-training for 30 epochs, while the regular-shaped dataset undergoes 50 epochs. The initial learning rates (LRs) for different networks have been determined through a meticulous manual search of parameters, the outcomes of which are detailed in the simulations and experimental results. The hyperparameters for the iterative approach IGGS are determined empirically. For all phantoms, the reconstruction results of the Tikhonov method with a 0.001 regularization factor are chosen as the initial point. The maximum number of iterations is set to 100, with a stopping tolerance of 1×10^{-7}. The optimization problem is addressed by utilizing the Accelerated Alternating Direction Method of Multipliers (A-ADMM). Additionally, the penalty parameters: η_1 and η_2, and multiplier update step lengths: ε_1 and ε_2, are selected based on the specific cases and they are detailed in the simulation and experiment section.

4. Simulation results and analysis

In this section, five competitive deep-learning networks and the IGGS method are selected as baselines to conduct a comprehensive evaluation. Both case study and whole test set analysis for the regular-shaped and lung-shaped EIT datasets are carried out. Furthermore, the robustness of the proposed SA-HFL against the measurement noise and modeling errors is examined. To assess the complexity of the networks, the model parameters and FLOPS are presented. Moreover, BBCE combined with MSE loss and solely MSE loss are employed to investigate the influence of weighted loss on conductivity distribution reconstruction performance.

4.1 Simulation results of regular-shaped EIT dataset

1) Case Study

Fig. 8 illustrates six representative cases along with their corresponding metrics.

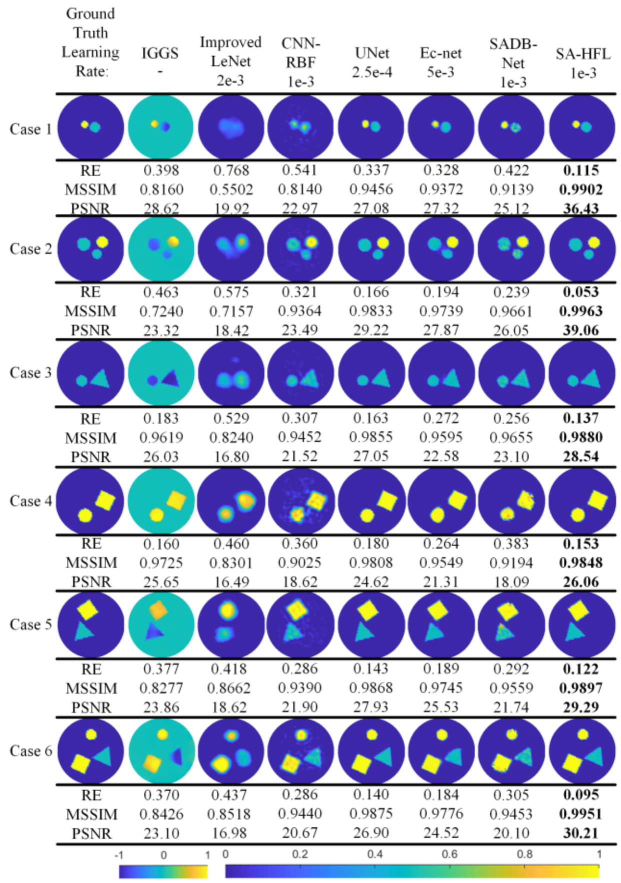

Fig. 8. Case analysis for the reconstruction of regular-shaped conductivity distribution under different methods.

In IGGS reconstructions, penalty parameters η_1 and η_2 as well as multiplier update step lengths ε_1 and ε_2 are set differently across various cases. For Cases 1 and 5, both η parameters are set to 0.0046 and both ε parameters are optimized to 0.504. In Cases 2 and 6, the η parameters are set to 0.004, with ε_1 and ε_2 parameters chosen as 1.46×10^{-4} and 0.1226, respectively. For Case 3, the η parameters take a value of 0.014, while ε parameters are set to 0.0319.

All methods are capable of reconstructing the targets. However, qualitative analysis indicates that the proposed SA-HFL exhibits minimal artifacts and precise object positions. Moreover, the three metrics employed also demonstrate superior performance among the six cases. By balancing BBCE and MSE loss, the SA-HFL effectively extracts the structural information and conductivity information of the target during training, so as to achieve accurate high-resolution conductivity reconstruction.

For Improved LeNet, CNN-RBF, Ec-Net, and SADB-Net, the lack of an encoder-decoder structure limits their capability to efficiently compress and reconstruct information, leading to suboptimal quality in conductivity reconstruction. The encoder-decoder architecture plays a crucial role in effectively integrating depth information from voltage data with shallow information, enabling more efficient extraction of EIT sensor information. Moreover, for Improved LeNet, CNN-RBF, and SADB-Net networks, the fully connected structure disrupts the spatial correlation between conductivity distribution. Besides,

Table 2
Average evaluation metrics for noiseless, regular-shaped data under different deep learning methods.

Methods	RE	MSSIM	PSNR
Improved LeNet [27]	0.486 ± 0.001	0.8147 ± 0.0013	18.01 ± 0.02
CNN-RBF [23]	0.313 ± 0.001	0.9346 ± 0.0004	21.79 ± 0.02
UNet [38]	0.165 ± 0.001	0.9809 ± 0.0003	27.90 ± 0.04
Ec-net [26]	0.221 ± 0.001	0.9659 ± 0.0004	25.19 ± 0.04
SADB-Net [29]	0.284 ± 0.001	0.9532 ± 0.0003	22.72 ± 0.03
SA-HFL	**0.119 ± 0.001**	**0.9882 ± 0.0002**	**31.03 ± 0.05**

Average ± standard error.

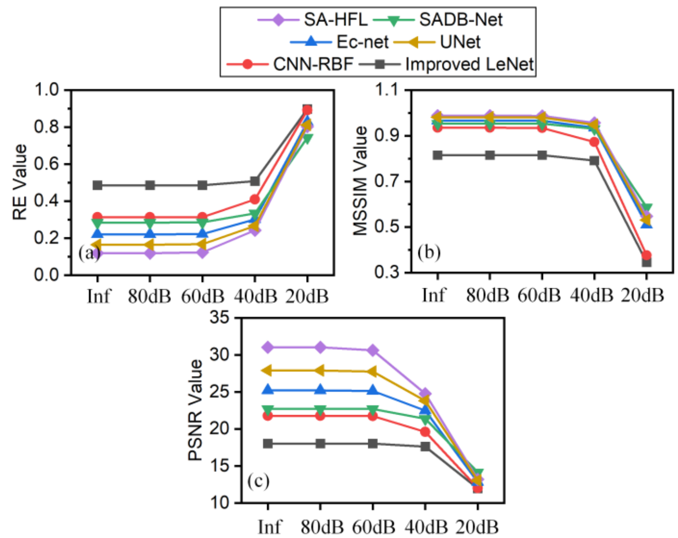

Fig. 9. Robustness analysis with respect to different SNR levels under different deep learning methods for the regular-shaped dataset. (a) RE, (b) MSSIM, (c) PSNR.

inadequate pre-training epochs and the inappropriate learning rate for the SADB-Net can result in the presence of gaps or holes in the reconstructed image. The reconstruction performance of UNet is suboptimal compared to the proposed network, largely because it lacks a segmentation branch for extracting structural information of the target. Moreover, IGGS underperforms when compared to SADB-Net, mainly due to the limitations of its linear model in solving the inverse problem itself.

In the regular-shaped EIT dataset, it is worth noting that a specific mapping is employed to assess metrics with the IGGS method due to its ability to reconstruct relative negative values. Specifically, a ground truth value of 0.5 is mapped to -1 for the comparison.

2) Test Set Analysis

The quantitative analysis results of the entire test set are listed in Table 2. The latter part denotes the standard error (SE), which is utilized to evaluate the uncertainty in the estimation of the mean. The table clearly demonstrates that the SA-HFL outperforms other methods in terms of RE, MSSIM, and PSNR. Specifically, the values are 0.119 ± 0.001, 0.9882 ± 0.0002, and 31.03 ± 0.05, respectively. When compared to the suboptimal UNet network, the SA-HFL exhibits a remarkable improvement with a 27.9% decrease in RE, a 0.7% increase in MSSIM, and an 11.2% increase in PSNR.

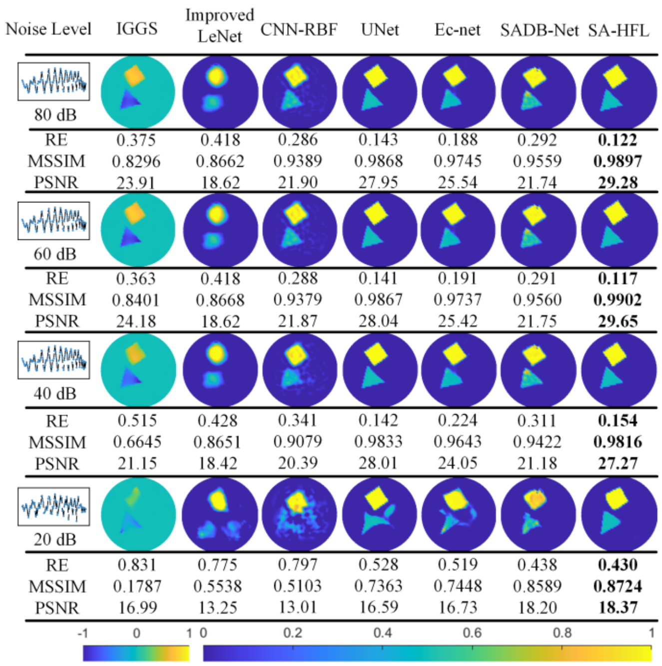

Fig. 10. Reconstruction of regular-shaped phantoms with different noise levels.

3) Robustness Analysis

A. Robustness Analysis to Measurement Noise: To assess the robustness of the proposed SA-HFL against measurement noise, GWN is incorporated into the boundary voltages of the test set at SNRs of 80 dB, 60 dB, 40 dB, and 20 dB. Results against SNRs for different methods are presented in Fig. 9. As the SNR decreases from infinity to 20 dB, all methods show a declining trend in terms of MSSIM and PSNR, while exhibiting an increasing trend in RE. The proposed algorithm demonstrates superior performance within a noise level range of 80 to 40 dB. However, a significant decline in performance metrics is observed for all methods when the noise level drops to 20 dB. In this scenario, the SADB-Net approach outperforms all others, relegating our method to a close second. This relative underperformance is primarily attributable to the absence of diverse noise levels in our training dataset, which compromises the predictive accuracy of the model under high-noise conditions.

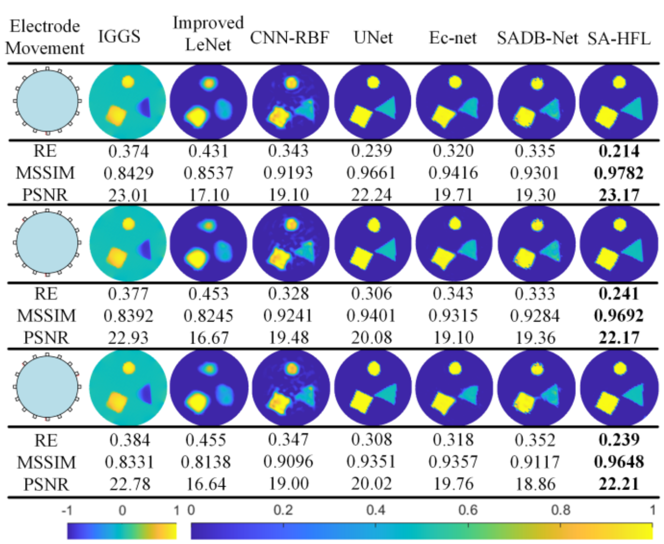

Fig. 11. Reconstruction of regular-shaped phantoms with electrode movements.

Fig. 10 presents the reconstruction results for Case 5 across varying noise levels. A discernible declining trend in image reconstruction quality is observed as noise levels increase. Nonetheless, both quantitative and qualitative analyses substantiate that the proposed SA-HFL method outperforms other competing approaches.

B. Robustness Analysis to Electrode Movement: Electrode movement is a primary source of modeling errors. To evaluate the robustness of various methods against electrode movement, tests are conducted based on Case 6 in which electrodes are rotated either clockwise or counterclockwise by an angular distance equal to 5% of the angle between adjacent electrodes. The electrode displacements and corresponding reconstruction results under different methods are displayed in Fig. 11. The position of the original electrode is represented by the red dotted line. In scenarios involving one to three electrode movements, the proposed method demonstrates superior performance over other deep learning methods and the IGGS method. Specifically, the proposed method yields reductions in RE of 10.5%, 21.2%, and 22.4% in the above three cases, compared to the next best method, UNet.

This finding indicates that deep-learning based reconstruction techniques effectively compensate for modeling errors caused by electrode movement. Additionally, the proposed method demonstrates superior robustness to such errors compared to other approaches.

C. Robustness Analysis to Domain Deformation: Domain deformation serves as another primary source of modeling errors. Fig. 12 illustrates the robustness of various methods against domain deformation based on Case 4. In this figure, the numbers in the first column represent the scaling ratios along the x and y axes of the circular domain, respectively. Both qualitative and quantitative analyses suggest that the proposed SA-HFL method surpasses other approaches, even though the

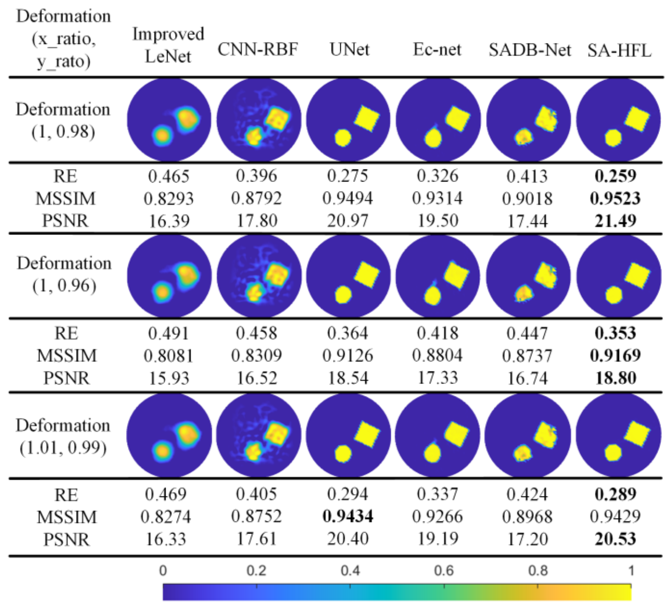

Fig. 12. Reconstruction of regular-shaped phantoms with domain deformation.

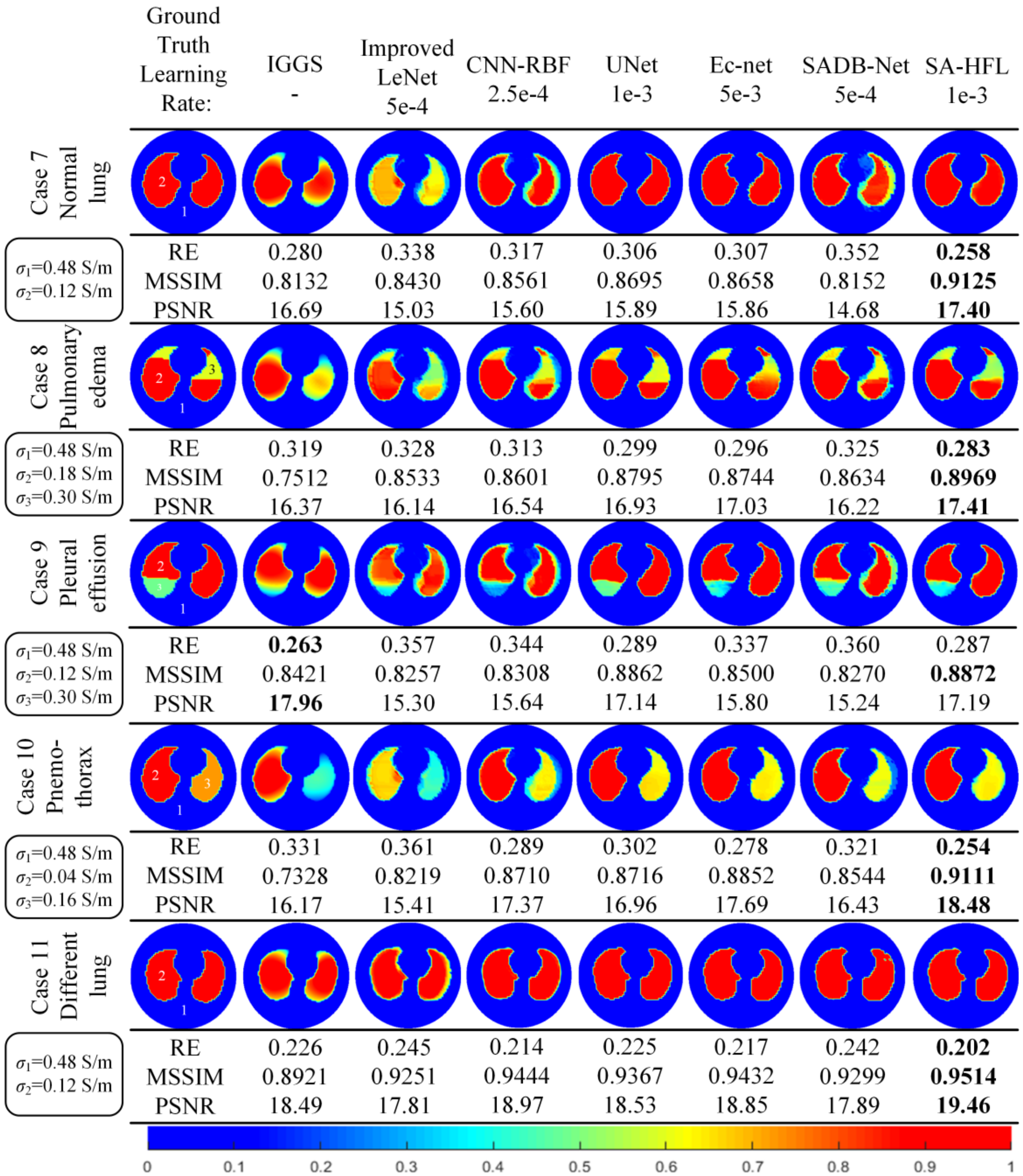

Case	Metric	IGGS	Improved LeNet	CNN-RBF	UNet	Ec-net	SADB-Net	SA-HFL
Case 7 (σ_1=0.48 S/m, σ_2=0.12 S/m)	RE	0.280	0.338	0.317	0.306	0.307	0.352	**0.258**
	MSSIM	0.8132	0.8430	0.8561	0.8695	0.8658	0.8152	**0.9125**
	PSNR	16.69	15.03	15.60	15.89	15.86	14.68	**17.40**
Case 8 (σ_1=0.48 S/m, σ_2=0.18 S/m, σ_3=0.30 S/m)	RE	0.319	0.328	0.313	0.299	0.296	0.325	**0.283**
	MSSIM	0.7512	0.8533	0.8601	0.8795	0.8744	0.8634	**0.8969**
	PSNR	16.37	16.14	16.54	16.93	17.03	16.22	**17.41**
Case 9 (σ_1=0.48 S/m, σ_2=0.12 S/m, σ_3=0.30 S/m)	RE	**0.263**	0.357	0.344	0.289	0.337	0.360	0.287
	MSSIM	0.8421	0.8257	0.8308	0.8862	0.8500	0.8270	**0.8872**
	PSNR	**17.96**	15.30	15.64	17.14	15.80	15.24	17.19
Case 10 (σ_1=0.48 S/m, σ_2=0.04 S/m, σ_3=0.16 S/m)	RE	0.331	0.361	0.289	0.302	0.278	0.321	**0.254**
	MSSIM	0.7328	0.8219	0.8710	0.8716	0.8852	0.8544	**0.9111**
	PSNR	16.17	15.41	17.37	16.96	17.69	16.43	**18.48**
Case 11 (σ_1=0.48 S/m, σ_2=0.12 S/m)	RE	0.226	0.245	0.214	0.225	0.217	0.242	**0.202**
	MSSIM	0.8921	0.9251	0.9444	0.9367	0.9432	0.9299	**0.9514**
	PSNR	18.49	17.81	18.97	18.53	18.85	17.89	**19.46**

Fig. 13. Case analysis for the reconstruction of lung-shaped conductivity distribution under different methods.

domain deformation can affect the reconstruction results. This suggests that SA-HFL effectively compensates for measurement errors induced by domain deformation, exhibiting superior robustness against domain deformation in comparison to other methods.

4.2 Simulation results of lung-shaped EIT dataset

1) Case Study

Five representative reconstruction results are shown in Fig. 13, where cases 7 to 11 correspond to a normal lung, three lung diseases, and a different lung shape. For the IGGS reconstruction results presented in Cases 7-11, the penalty parameters η_1 and η_2 are set as 0.012 and 0.004, respectively. The update step lengths for the multipliers, ε_1, and ε_2, are optimized as 3.4×10^{-3} and 3.4×10^{-3}.

The analysis results of the lung-shaped dataset are consistent with those of the regular-shaped dataset, further demonstrating the superior performance of the proposed SA-HFL in both quantitative and qualitative analyses.

The disparities in conductivity reconstruction performance can be attributed to variations in network depths and learning capabilities. Overall, the proposed SA-HFL surpasses other deep learning methods in both quantitative analyses, encompassing RE, MSSIM, and PSNR, and qualitative analysis, including the presence of artifacts and visual disparities compared to the ground truth. The SA-HFL demonstrates its potential in capturing and reflecting lung diseases in the reconstructed images.

Table 3
Average evaluation metrics for noiseless, lung-shaped data under different deep learning methods.

Methods	RE	MSSIM	PSNR
Improved LeNet	0.309 ± 0.002	0.8708 ± 0.0008	17.14 ± 0.04
CNN-RBF	0.277 ± 0.001	0.8916 ± 0.0007	18.04 ± 0.04
UNet	0.275 ± 0.001	0.9032 ± 0.0005	18.07 ± 0.03
Ec-net	0.273 ± 0.001	0.9002 ± 0.0005	18.15 ± 0.04
SADB-Net	0.289 ± 0.001	0.8830 ± 0.0007	17.62 ± 0.04
SA-HFL	**0.257 ± 0.001**	**0.9151 ± 0.0004**	**18.67 ± 0.04**

Average ± standard error.

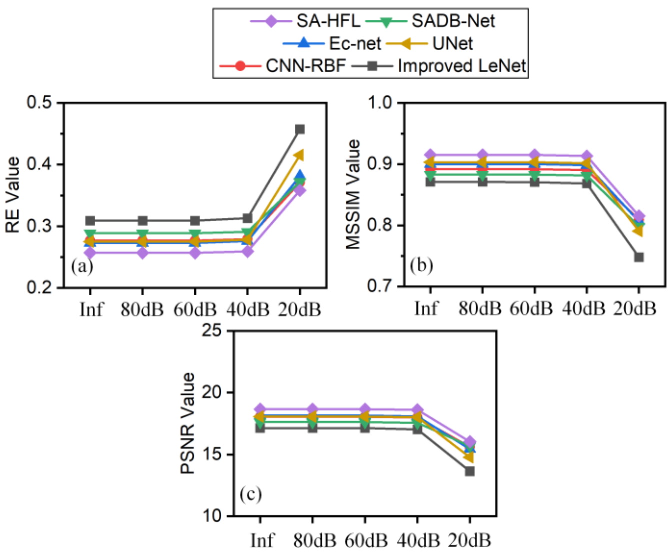

Fig. 14. Robustness analysis with respect to different SNR levels under different deep learning methods for the lung-shaped dataset. (a) RE, (b) MSSIM, (c) PSNR.

It should be mentioned that to facilitate the comparison, the conductivity reconstruction results have been mapped between 0 and 1. Therefore, the lung images depicted in Fig. 13 represent relative conductivity. The absolute conductivity values are provided on the left side of the figure.

2) Test Set Analysis

The quantitative analysis results of the test set are presented in Table 3, with the best results highlighted in bold. The proposed SA-HFL outperforms other methods in terms of RE, MSSIM, and PSNR, achieving a value of 0.257 ± 0.001, 0.9151 ± 0.0004, and 18.67 ± 0.04, respectively.

3) Robustness Analysis

A. Robustness Analysis to Measurement Noise: Similarly, 80 dB, 60 dB, 40 dB, and 20 dB SNRs are added to the measurement voltages in the lung-shaped EIT dataset. The robustness analysis results against SNRs for different methods are presented in Fig. 14. As the SNR decreases from infinity to 20 dB, all methods show a declining trend in terms of MSSIM and PSNR, while exhibiting an increasing trend in RE. However, all methods demonstrate a certain level of robustness against the SNR, particularly the proposed SA-HFL, which maintains the highest conductivity reconstruction capability even at lower SNR levels. This suggests that the hybrid-fusion learning network effectively leverages multi-scale information, including structural and conductivity distribution information, from different branches. This approach mitigates the issue of limited informative features extracted by single-branch networks, resulting in improved reconstruction performance and enhanced robustness to measurement noise in the training model.

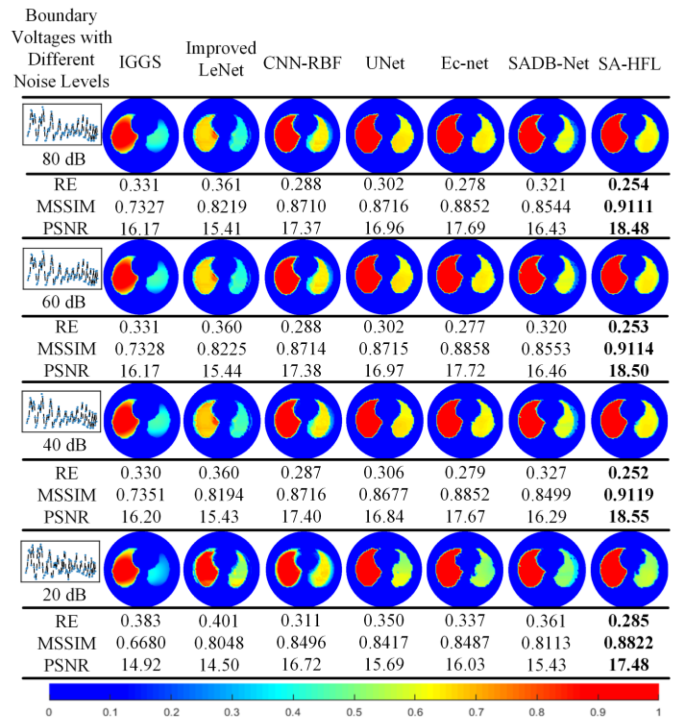

Fig. 15. Reconstruction of lung-shaped phantoms with different noise levels.

The reconstruction results for Case 10 under different noise levels are displayed in Fig. 15. The figure clearly indicates that although the quality of image reconstruction shows a deteriorating trend as noise levels increase, the proposed method still outperforms other methods in terms of RE, MSSIM, and PSNR metrics.

B. Robustness Analysis to Electrode Movement: Using Case 7 as a basis, the outcomes of the robustness against electrode movements are shown in Fig. 16 and 17. Specifically, Fig. 16 adheres to the same test protocol used for robustness analysis with the regular-shaped dataset, wherein electrodes are rotated either clockwise or counterclockwise with an angular shift that is 5% of the angular distance between neighboring electrodes. In real medical applications, the placement of EIT electrodes may not always strictly follow clinical guidelines. To account for such scenarios, a robustness analysis involving larger electrode movements is conducted for the lung-shaped EIT dataset and the results are presented in Fig. 17. In the case of single-electrode movement, the electrode is rotated by an angular distance of 22.2% between the electrodes. For cases involving the movement of two or three electrodes, the angular rotation distance is set at 11.1%. Based on the quantitative analysis presented in Fig. 16 and 17, the evaluation metrics for the proposed network outperform those of competing methods. The average RE across the six cases decreased by 9.6% relative to the second-best performing method, while the MSSIM increased by 2.4% and the PSNR improved by 4.8%.

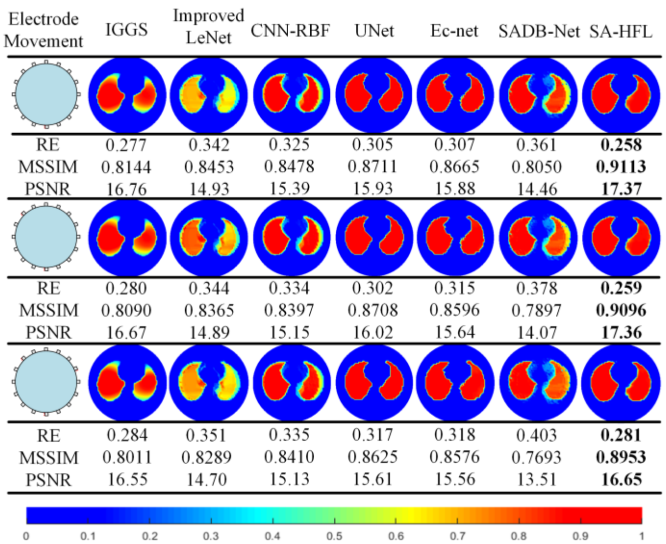

Fig. 16. Reconstruction of lung-shaped phantoms with electrode movements.

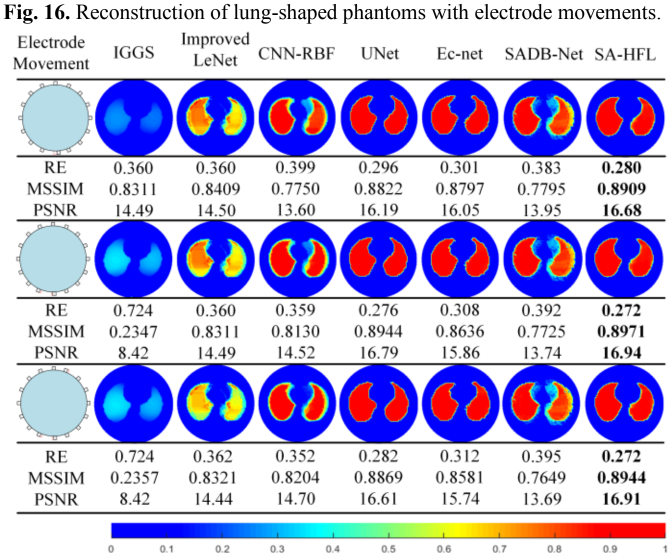

Fig. 17. Reconstruction of lung-shaped phantoms with greater electrode movement offsets.

C. Robustness Analysis to Domain Deformation: Similarly, a robustness analysis for domain deformation on the lung-shaped dataset under various deep learning methods is conducted. The results are presented in Fig. 18, and the conclusions drawn are in alignment with those from the regular-shaped dataset analysis.

4) Thorax Domain

To evaluate the performance of networks for the shape of the thorax domain, a specialized EIT dataset is created. This dataset features 18 lung shapes, with each case corresponding to a normal lung condition. The training set comprises 7,056 samples, while the test set contains 882. The reconstruction results for selected cases are illustrated in Fig. 19. For these cases, the metrics of the proposed SA-HFL surpass those achieved by other deep learning results and the IGGS method. For the IGGS method, the penalty parameters η_1 and η_2 are configured as 0.08 and 0.02, respectively. Additionally, the multiplier update step lengths, ε_1, and ε_2, are chosen as 1×10^{-3} and 0.025.

Table 4 lists the average evaluation metrics for noise-free, lung-shaped data in the thorax domain, benchmarked against

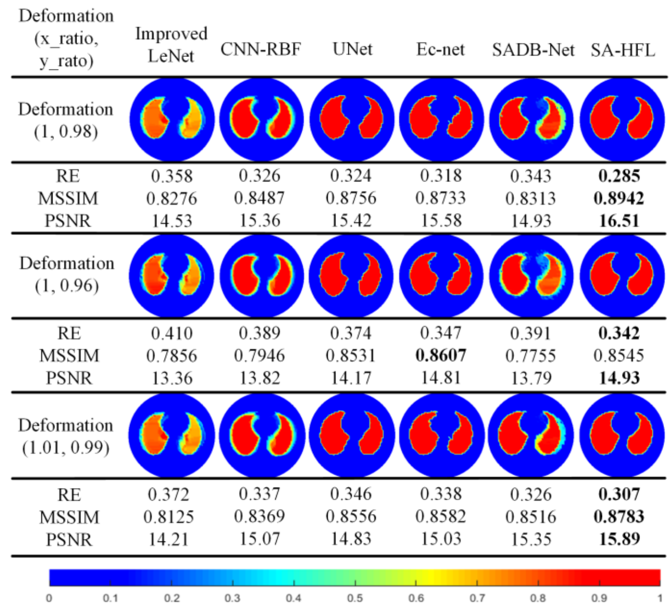

Fig. 18. Reconstruction of lung-shaped phantoms with domain deformation.

various deep learning methodologies and the IGGS method. Our proposed network excels in all metrics, registering a RE of 0.252 ± 0.001, an MSSIM of 9128 ± 0.0008, and a PSNR of 15.61 ± 0.05. These results substantiate that our proposed network not only performs optimally in the circular domain but also demonstrates superior results in the thoracic domain.

4.3 Model parameters and FLOPS

The model parameters and FLOPs are listed in Table 5 to assess the complexity of different networks. Although the proposed SA-HFL does not achieve optimal results in terms of

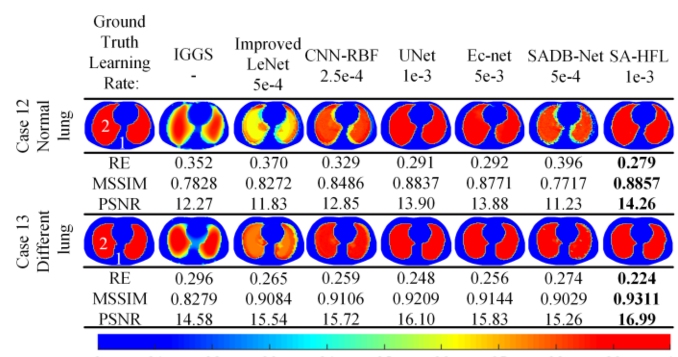

Fig. 19. Case analysis for the reconstruction of lung-shaped conductivity distribution for the thorax domain under different methods. σ_1=0.48 S/m, σ_2=0.12 S/m

Table 4
Average evaluation metrics for noiseless, lung-shaped data in the thorax domain under different deep learning methods.

Methods	RE	MSSIM	PSNR
Improved LeNet	0.313 ± 0.002	0.8746 ± 0.0014	13.83 ± 0.07
CNN-RBF	0.297 ± 0.001	0.8846 ± 0.0011	14.22 ± 0.05
UNet	0.269 ± 0.001	0.9081 ± 0.0007	15.03 ± 0.04
Ec-net	0.274 ± 0.001	0.9011 ± 0.0008	14.87 ± 0.04
SADB-Net	0.338 ± 0.002	0.8429 ± 0.0022	13.17 ± 0.07
SA-HFL	**0.252 ± 0.001**	**0.9128 ± 0.0008**	**15.61 ± 0.05**

Average ± standard error.

Table 5

Parameters and flops for different models.

Methods	Parameters (M)	FLOPs (G)
Improved LeNet	7.42	**0.0157**
CNN-RBF	3.98	0.047
UNet	2.38	1.335
Ec-net	**0.45**	0.134
SADB-Net	48.19	5.416
SA-HFL	6.56	1.487

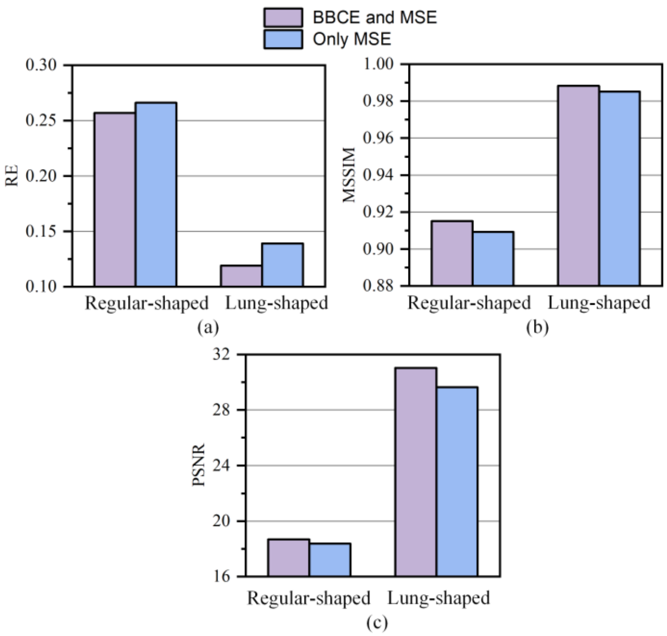

Fig. 20. Average metrics under different loss functions. (a) RE, (b) MSSIM, (c) PSNR.

these metrics, the metrics are moderately ranked, suggesting that the SA-HFL strikes a suitable balance between the number of parameters and network complexity.

Among the baseline models, the Ec-net has the fewest parameters, totaling 0.45 million, while the Improved LeNet model achieves the lowest FLOPs, with 0.0157 billion floating-point operations. Furthermore, except the IGGS iterative method, which costs 0.0197s to reconstruct the conductivity distribution, all methods managed to achieve a frame rate of 40 frames per second (fps) on a Windows laptop. As for the proposed SA-HFL method, it was able to achieve 49.5 fps, which is fast enough for real-time inference [42].

4.4 Different loss functions

In the paper, different loss functions, including weighted BBCE and MSE, as well as only MSE, are utilized to evaluate the impact of the combined loss function on the conductivity reconstruction performance in the two EIT datasets. The average metrics are presented in the Fig. 20.

From the paper, it is evident that when employing only the MSE as the loss function, the RE increases from 0.119 to 0.139 on the regular-shaped dataset and from 0.257 to 0.266 on the lung-shaped dataset, in comparison to the weighted loss function. Additionally, the MSSIM decreases from 0.9882 to 0.9851 and from 0.9151 to 0.9092, respectively. Moreover, the PSNR exhibits a decline from 31.03 to 29.65 on the regular-shaped dataset and from 18.67 to 18.37 on the lung-shaped dataset. This reveals that in the EIT reconstruction task, the structural information and conductivity information of the reconstruction target can be fused through the weighted loss function, thereby improving the accuracy of reconstruction.

5. Experimental results and analysis

5.1 Experiment setup

To assess the performance of the proposed network and its ability to practice application for lung ventilation, data from three distinct EIT experiments were utilized.

In the first experiment, the open-source 2D EIT dataset was employed to scrutinize the reconstruction efficacy of the proposed network [43]. The frequency range for the KIT4 EIT system could range from 1 kHz to 120 kHz, with the system comprising five layers, each equipped with 16 electrodes. The EIT system demonstrated maximum and minimum SNR of 97.5 dB and 59.3 dB respectively, achieving a frame rate of 31.25 fps. Furthermore, in assessing the stability of the system, a five-hour-long measurement of a resistive object revealed that the changes in voltage corresponded to the order of the noise level [44]. The dataset was obtained from a circular tank with a radius of 14cm, outfitted with 16 uniformly distributed electrodes. The tank was filled with tap water to a height of 7cm, which possessed a conductivity of 0.06 S/m. An excitation current characterized by a magnitude of 2mA and a frequency of 1kHz was applied. A variety of regular-shaped inclusions, both metallic and insulated, were placed in the water tank.

The second experiment utilized the Edinburgh EIT system. The Edinburgh EIT system has 32 electrode interfaces and operates within a frequency range of 10 kHz to 1 MHz. The maximum and minimum SNR recorded were 82.82 dB and 45.51 dB respectively, with the system achieving a maximum frame rate of 546 fps at 625 kHz in serial mode. Importantly, the EIT system demonstrated robust performance in both 2D and 3D time-difference and frequency-difference imaging. More detailed information is described in [45]. In the experiment, a non-conductive cylinder crafted from black resin was placed in a miniature EIT sensor, measuring 7 mm in height and 15 mm in diameter. The frequency of the excitation current was set at 10 kHz, and the amplitude of the injected current was approximately 1.5 mA peak to peak. The background conductivity was set at 1.898 S/m.

The third experiment utilized EIT data from healthy human shallow breathing, obtained from EIDORS, an open EIT community.

5.2 Experimental results

The reconstruction results for the first experiment are presented in Fig. 21, where the MSSIM for six test cases is also included. When compared to the IGGS method and other deep learning methods, the SA-HFL method exhibits fewer artifacts and offers superior accuracy in imaging the target, as evidenced by the improved MSSIM metric. As the last layer of Improved

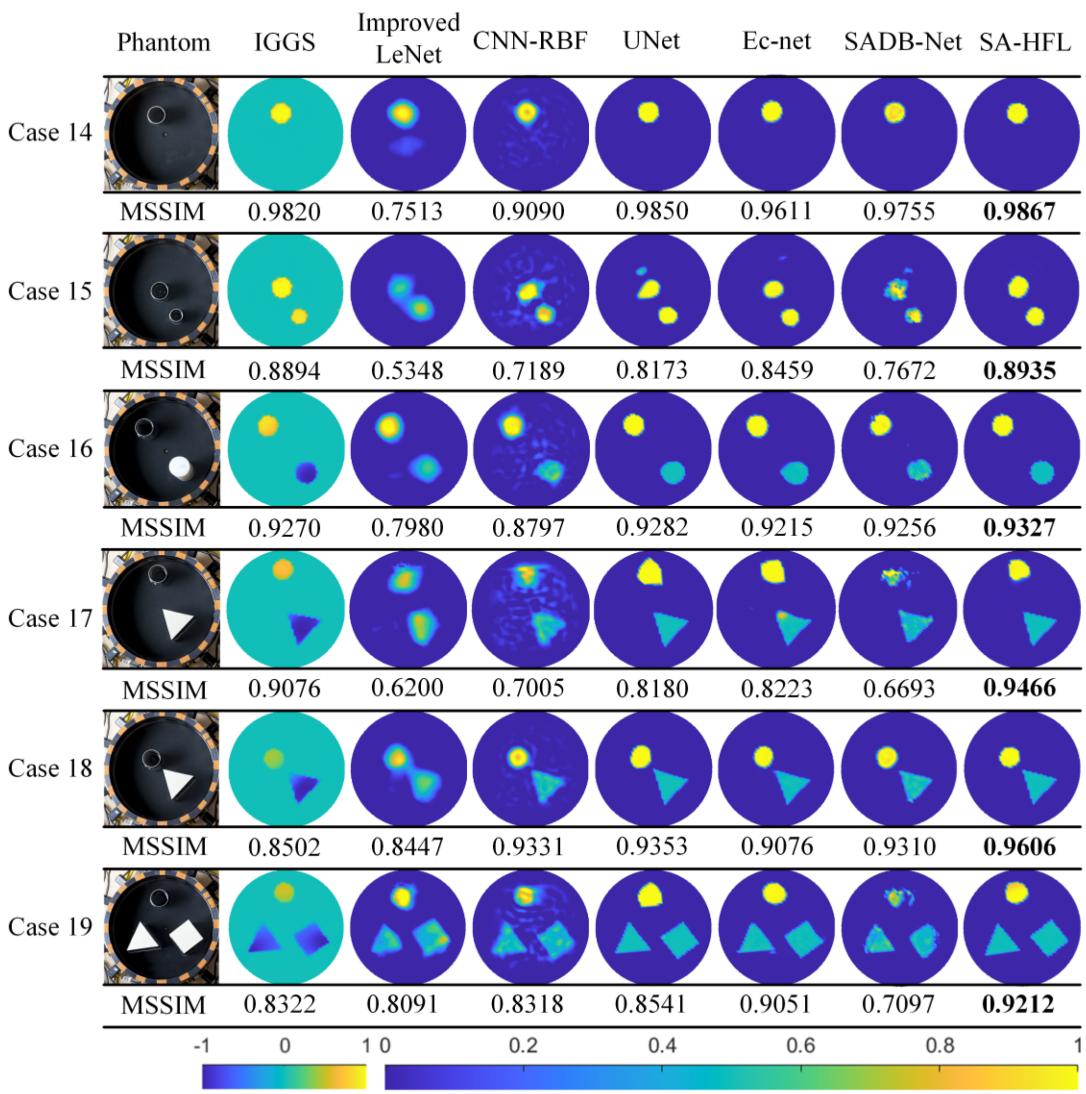

Fig. 21. Reconstruction results of six test cases in the first experiment.

LeNet, CNN-RBF, and SADB-Net utilizes a fully connected layer, this disrupts the spatial correlation of the conductivity distribution, which leads to the generation of artifacts and sub-optimal reconstruction quality. Furthermore, the SADB-Net network employs LeNet as its information extraction component. Due to the inherent shallowness of this architecture, it yields sub-optimal reconstruction quality. The performance of Ec-net and UNet, in terms of reconstruction results, demonstrates slight underperformance when compared with the proposed network, due to their no utilization of the binary mask information in the data. In contrast, the proposed SA-HFL learns the structural information of the data by combining BBCE and MSE as the weighted loss function, therefore enhancing the learning efficacy.

Fig. 22 presents the results of the second experiment. Given the complexity of the manufacturing process of the miniature EIT sensor, the data collected are more susceptible to external interference. This leads to the appearance of blue spots in some reconstructed images. Despite this limitation, it is evident that the proposed SA-HFL outperforms other networks in terms of reconstruction quality. For Case 21, IGGS achieves a marginally higher MSSIM compared to SA-HFL. This superior performance of IGGS is primarily attributed to the incorporation of strong optical image prior information. However, even in the absence of an optical image, SA-HFL is still capable of accurately reconstructing the position of the resin and outperforms other deep learning methods in terms of the MSSIM metric.

All parameter settings for the IGGS method are listed in Table 6.

To validate the clinical applicability of the proposed method, real healthy human lung EIT data in our third experiment are employed. The corresponding results are illustrated in Fig. 23. As a benchmark for assessing the respiratory state, the

Table 6

Parameter settings for the experiment results of the IGGS method.

Case	Penalty parameters: η_1 and η_2	Multiplier update step lengths: ε_1 and ε_2
Case 14, 15, 20, 21	0.016, 0.016	0.089, 0.089
Case 16, 17, 18	0.04, 0.04	0.0168, 0.0168
Case 19	2×10^{-4}, 2×10^{-4}	3×10^{-5}, 0.0168

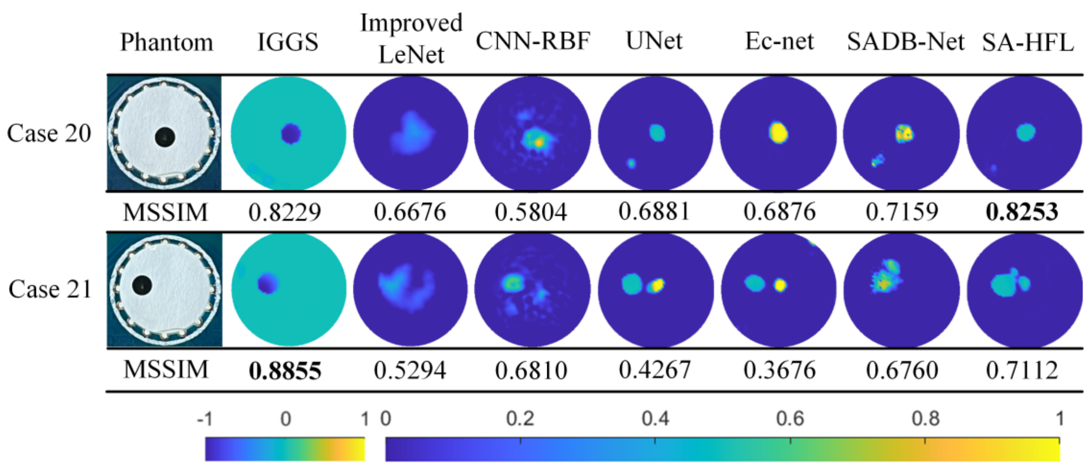

Fig. 22. Reconstruction results of two test cases in the second experiment.

Tikhonov regularization method was utilized, with the regularization parameter set as 0.005. As evidenced by the results presented in Fig. 23, our proposed algorithm demonstrates its efficacy by reconstructing the shape of the lung. Furthermore, the observed changes in respiratory state are found to be in close agreement with those obtained via the Tikhonov method, substantiating the applicability of our method to real human lung data.

Three experimental studies have provided evidence for the effectiveness and superiority of the EIT method when combined with deep learning, opening up possibilities for medical imaging.

6. Conclusion

In this study, a supervised SA-HFL deep learning method was proposed to reconstruct high-resolution conductivity and improve robustness against measurement noise and modeling errors. Through simulations and experiments, the effectiveness of the network was proven and compared with five deep learning methods and the optical image-guided group sparsity (IGGS) method. The evaluation metrics (RE, MSSIM, and PSNR) clearly improved with the SA-HFL method, with values of 0.119, 0.9882, and 31.03 for the regular-shaped dataset, and 0.257, 0.9151, and 18.67 for the lung-shaped dataset, respectively. The results also highlight the significant enhancement in reconstruction accuracy achieved by fusing structural information and conductivity information of the reconstructed object using a weighted loss function. This study explores the application of combining EIT with deep learning for lung reconstruction, expanding the potential of EIT in medicine. Future research will focus on advancing 3D EIT reconstruction techniques for lung imaging.

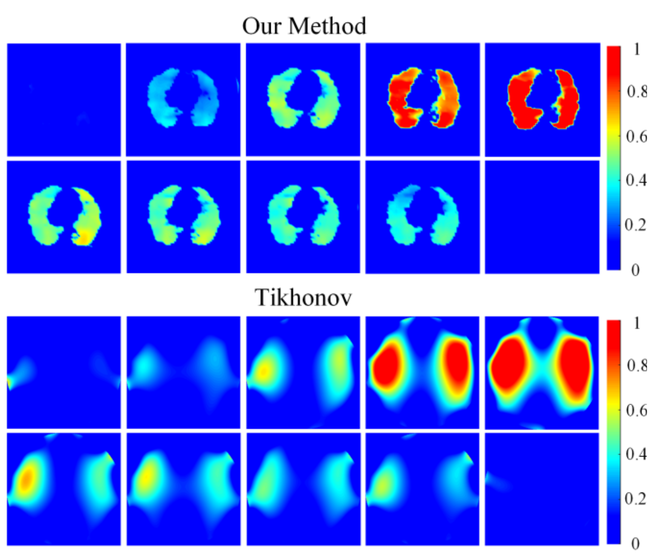

Fig. 23. Reconstruction results of shallow breathing in a healthy human.

References

[1] M. Mosing, U. Auer, P. Macfarlane, D. Bardell, Regional ventilation distribution and dead space in anaesthetized horses treated with and without continuous positive airway pressure: novel insights by electrical impedance tomography and volumetric capnography, Vet. Anaesth. Analg. 45 (1) (2018) 31–40.

[2] F.D.S. Rossi, I.A. Cristina, Z. Yagui, I.L.B. Haddad, I.A.D.A. Deutsch, Electrical impedance tomography to evaluate air distribution prior to extubation in very-low-birth-weight infants: a feasibility study, Clinics. 68 (3) (2013) 345–350.

[3] T. Riva, F. Pascolo, M. Huber, L. Theiler, R. Greif, N. Disma, A. Fuchs, J. Berger-estilita, T. Riedel, Evaluation of atelectasis using electrical impedance tomography during procedural deep sedation for MRI in small children: A prospective observational trial, J. Clin. Anesth. 77 (2022) 110626.

[4] T. Liu, J. Ruan, J. Rong, W. Hao, W. Li, Cone-beam X-ray luminescence computed tomography based on MLEM with adaptive FISTA initial image, Comput. Methods Programs Biomed. 229 (2023) 107265.

[5] C.G. Xanthis, D. Filos, K. Haris, A.H. Aletras, Simulator-generated training datasets as an alternative to using patient data for machine learning: An example in myocardial segmentation with MRI, Comput. Methods Programs Biomed. 198 (2021) 105817.

[6] L. Yang, Z. Li, M. Dai, F. Fu, K. Möller, Y. Gao, Z. Zhao, Optimal machine learning methods for prediction of high-flow nasal cannula outcomes using image features from electrical impedance tomography, Comput. Methods Programs Biomed. 238 (2023) 107613.

[7] T. Bluth, T. Kiss, M. Kircher, A. Braune, C. Bozsak, R. Huhle, M. Scharffenberg, M. Andreeff, T. Koch, M. Herzog, J. Roegner, P. Herzog, L. Vivona, M. Millone, O. D, J. Kotzerke, B. Stender, M.G. De Abreu, Measurement of relative lung perfusion with electrical impedance and positron emission tomography : an experimental comparative study in pigs, Br. J. Anaesth. 123 (2) (2019) 246–254.

[8] N. Strodthoff, C. Strodthoff, T. Becher, N. Weiler, I. Frerichs, Inferring respiratory and circulatory parameters from electrical impedance tomography with deep recurrent models, IEEE J. Biomed. Heal. Informatics. 25 (8) (2020) 3105–3111.

[9] K. Zhang, R. Guo, M. Li, F. Yang, S. Xu, A. Abubakar, Supervised Descent Learning for Thoracic Electrical Impedance Tomography, IEEE Trans. Biomed. Eng. 68 (4) (2021) 1360–1369.

[10] M. Balleza-ordaz, E. Alday-perez, M. Vargas-luna, S. Kashina, M.R. Huerta-franco, Tidal volume monitoring by a set of tetrapolar impedance measurements selected from the 16-electrodes arrangement used in electrical impedance tomography (EIT) technique. Calibration equations in a group of healthy males, Biomed. Signal Process. Control. 27 (2016) 68–76.

[11] T. Rymarczyk, B. Stefaniak, K. Kania, M. Maj, P. Nita, Inverse Problem Solution for Model with Lungs and Heart in EIT, in: 2019 Appl. Electromagn. Mod. Eng. Med., IEEE, 2019: pp. 180–183.

[12] H. Yu, Z. Zhang, Y. Gao, J. Jia, Multiscale voltage reconstruction with attention-based network for volume fraction prediction of industrial oil-water two-phase flow by EIT, IEEE Trans. Instrum. Meas. 71 (2022) 1–9.

[13] M. Jehl, J. Avery, E. Malone, D. Holder, T. Betcke, Correcting electrode modelling errors in EIT on realistic 3D head models, Physiol. Meas. 36 (12) (2015) 2423–2442.

[14] B. Gong, B. Schullcke, S. Krueger-Ziolek, F. Zhang, U. Mueller-Lisse, K. Moeller, Higher order total variation regularization for EIT reconstruction, Med. Biol. Eng. Comput. 56 (8) (2018) 1367–1378.

[15] S. Liu, J. Jia, Y.D. Zhang, Y. Yang, Image Reconstruction in Electrical Impedance Tomography Based on Structure-Aware Sparse Bayesian Learning, IEEE Trans. Med. Imaging. 37 (9) (2018) 2090–2102.

[16] M. Lukaschewitsch, P. Maass, M. Pidcock, Tikhonov regularization for electrical impedance tomography on unbounded domains, Inverse Probl. 19 (3) (2003) 585–610.

[17] Y. Wang, F. Dong, S. Ren, Computational Focusing Sensor: Enhancing Spatial Resolution of Electrical Impedance Tomography in Region of Interest, IEEE Sens. J. 21 (17) (2021) 19101–19111.

[18] S.J. Hamilton, A. Hauptmann, Deep D-Bar: Real-Time Electrical Impedance Tomography Imaging With Deep Neural Networks, IEEE Trans. Med. Imaging. 37 (10) (2018) 2367–2377.

[19] X. Chen, Z. Wang, X. Zhang, R. Fu, D. Wang, M. Zhang, H. Wang, Deep Autoencoder Imaging Method for Electrical Impedance Tomography, IEEE Trans. Instrum. Meas. 70 (2021) 1–15.

[20] X. Li, R. Zhang, Q. Wang, X. Duan, Y. Sun, J. Wang, SAR-CGAN: Improved generative adversarial network for EIT reconstruction of lung diseases, Biomed. Signal Process. Control. 81 (2023) 104421.

[21] K. Grzegorz, A. Ho, T. Rymarczyk, M. Mazurek, K. Niderla, M. Rzemieniak, Use of the double-stage LSTM network in electrical tomography for 3D wall moisture imaging, Measurement. 213 (2023) 112741.

[22] Z. Wei, D. Liu, X. Chen, Dominant-Current Deep Learning Scheme for Electrical Impedance Tomography, IEEE Trans. Biomed. Eng. 66 (9) (2019) 2546–2555.

[23] Y. Wu, B. Chen, K. Liu, C. Zhu, H. Pan, J. Jia, H. Wu, J. Yao, Shape Reconstruction With Multiphase Conductivity for Electrical Impedance Tomography Using Improved Convolutional Neural Network Method, IEEE Sens. J. 21 (7) (2021) 9277–9287.

[24] Z. Chen, Y. Yang, J. Jia, P. Bagnaninchi, Deep Learning Based Cell Imaging with Electrical Impedance Tomography, in: 2020 IEEE Int. Instrum. Meas. Technol. Conf., IEEE, 2020: pp. 1–6.

[25] S. Ren, K. Sun, C. Tan, F. Dong, A Two-Stage Deep Learning Method for Robust Shape Reconstruction With Electrical Impedance Tomography, IEEE Trans. Instrum. Meas. 69 (7) (2020) 4887–4897.

[26] Q. Wang, H. Zhang, X. Li, X. Duan, J. Wang, R. Zhang, H. Zhang, Y. Ma, H. Wang, J. Jia, Error-Constraint Deep Learning Scheme for Electrical Impedance Tomography (EIT), IEEE Trans. Instrum. Meas. 71 (2022) 1–11.

[27] C. Tan, S. Lv, F. Dong, M. Takei, Image Reconstruction Based on Convolutional Neural Network for Electrical Resistance Tomography, IEEE Sens. J. 19 (1) (2019) 196–204.

[28] A. Bianchessi, R.H. Akamine, G.C. Duran, N. Tanabi, A.K. Sato, T.C. Martins, M.S.G. Tsuzuki, Electrical Impedance Tomography Image Reconstruction Based on Neural Networks, IFAC-PapersOnLine. 53 (2) (2020) 15946–15951.

[29] Z. Chen, Y. Yang, Structure-Aware Dual-Branch Network for Electrical Impedance Tomography in Cell Culture Imaging, IEEE Trans. Instrum. Meas. 70 (2021) 1–9.

[30] Z. Liu, Y. Yang, Image Reconstruction of Electrical Impedance Tomography Based on Optical Image-Guided Group Sparsity, IEEE Sens. J. 21 (19) (2021) 21893–21902.

[31] E. Somersalo, M. Cheney, D. Isaacson, Existence and Uniqueness for Electrode Models for Electric Current Computed Tomography, SIAM J. Appl. Math. 52 (4) (1992) 1023–1040.

[32] D. Gu, D. Liu, D. Smyl, J. Deng, J. Du, Supershape Recovery From Electrical Impedance Tomography Data, IEEE Trans. Instrum. Meas. 70 (2021) 1–11.

[33] Guoya Dong, J. Zou, R.H. Bayford, Xinshan Ma, Shankai Gao, Weili Yan, Manling Ge, The comparison between FVM and FEM for EIT forward problem, IEEE Trans. Magn. 41 (5) (2005) 1468–1471.

[34] M.-H. Guo, C.-Z. Lu, Z.-N. Liu, M.-M. Cheng, S.-M. Hu, Visual Attention Network, (2022) 1–21. http://arxiv.org/abs/2202.09741.

[35] D. Hendrycks, K. Gimpel, Gaussian Error Linear Units (GELUs), (2016) 1–9. http://arxiv.org/abs/1606.08415.

[36] W. Wang, E. Xie, X. Li, D.-P. Fan, K. Song, D. Liang, T. Lu, P. Luo, L. Shao, PVTv2: Improved Baselines with Pyramid Vision Transformer, Comput. Vis. Media. 8 (3) (2022) 415-424.

[37] J.L. Ba, J.R. Kiros, G.E. Hinton, Layer Normalization, (2016). http://arxiv.org/abs/1607.06450.

[38] O. Ronneberger, P. Fischer, T. Brox, U-Net: Convolutional Networks for Biomedical Image Segmentation, (2015). https://arxiv.org/abs/1505.045972.

[39] S. Xie, Z. Tu, Holistically-Nested Edge Detection, in: 2015 IEEE Int. Conf. Comput. Vis., IEEE, 2015: pp. 1395–1403.

[40] S.D. Donal, Pleural Effusion : A Diagnostic Dilemma, Jama. 236 (19) (1976) 2183–2186.

[41] Q. Wang, J. Wang, X. Li, X. Duan, R. Zhang, H. Zhang, Y. Ma, H. Wang, J. Jia, Exploring Respiratory Motion Tracking Through Electrical Impedance Tomography, IEEE Trans. Instrum. Meas. 70 (2021) 1–12.

[42] B. Gong, S. Krueger-ziolek, K. Moeller, B. Schullcke, B. Gong, S. Krueger-ziolek, Electrical impedance tomography : functional lung imaging on its way to clinical practice?, Expert Rev. Resp. Med. 9 (6) (2015) 721–737.

[43] A. Hauptmann, V. Kolehmainen, N.M. Mach, T. Savolainen, A. Seppänen, S. Siltanen, Open 2D Electrical Impedance Tomography data archive, (2017) 1–15. http://arxiv.org/abs/1704.01178.

[44] J. Kourunen, T. Savolainen, A. Lehikoinen, M. Vauhkonen, L.M. Heikkinen, Suitability of a PXI platform for an electrical impedance tomography system, Meas. Sci. Technol. 20 (1) (2009) 015503.

[45] Y. Yang, J. Jia, A multi-frequency electrical impedance tomography system for real-time 2D and 3D imaging, Rev. Sci. Instrum. 88 (8) (2017) 085110.